Biophysical Chemistry 315 (2024) 107329

Contents lists available at ScienceDirect

Biophysical Chemistry

journal homepage: www.elsevier.com/locate/biophyschem

Structural changes of *Natronomonas pharaonis* halorhodopsin in its late photocycle revealed by solid-state NMR spectroscopy

Xin Zhang [a], Hajime Tamaki [a], Takashi Kikukawa [b], Toshimichi Fujiwara [a], Yoh Matsuki [a,c,*]

[a] Institute for Protein Research, Osaka University, Japan
[b] Faculty of Advanced Life Science, Hokkaido University, Japan
[c] Center for Quantum Information and Quantum Biology, Osaka University, Japan

ARTICLE INFO

Keywords:
Solid-state NMR spectroscopy
Dynamic nuclear polarization
Flash-photolysis
Halorhodopsin
Trimer assembly
Chloride ion transport

ABSTRACT

Natronomonas pharaonis halorhodopsin (*Np*HR) is a light-driven Cl^- inward pump that is widely used as an optogenetic tool. Although *Np*HR is previously extensively studied, its Cl^- uptake process is not well understood from the protein structure perspective, mainly because in crystalline lattice, it has been difficult to analyze the structural changes associated with the Cl^- uptake process. In this study, we used solid-state NMR to analyze *Np*HR both in the Cl^--bound and -free states under near-physiological transmembrane condition. Chemical shift perturbation analysis suggested that while the structural change caused by the Cl^- depletion is widespread over the *Np*HR molecule, residues in the extracellular (EC) part of helix D exhibited significant conformational changes that may be related to the Cl^- uptake process. By combining photochemical analysis and dynamic nuclear polarization (DNP)-enhanced solid-state NMR measurement on *Np*HR point mutants for the suggested residues, we confirmed their importance in the Cl^- uptake process. In particular, we found the mutation at Ala165 position, located at the trimer interface, to an amino acid with bulky sidechain (A165V) significantly perturbs the late photocycle and disrupts its trimeric assembly in the Cl^--free state as well as during the ion-pumping cycle under the photo-irradiated condition. This strongly suggested an outward movement of helix D at EC part, disrupting the trimer integrity. Together with the spectroscopic data and known *Np*HR crystal structures, we proposed a model that this helix movement is required for creating the Cl^- entrance path on the extracellular surface of the protein and is crucial to the Cl^- uptake process.

1. Introduction

Halorhodopsin (HR) is a member of the retinylidene protein family, which utilizes light energy to transport halide ions into cells [1]. This light-induced halide ion influx is known to be necessary for energy generation and/or for maintaining osmotic pressure balance [2]. Since HR was first discovered and recognized as light-driven Cl^- pump in 1980s from halophilic archaea [1,3,4], many other HRs were found in archaea and marine microorganisms that share similar structural characteristics [5]. HRs consists of a seven-transmembrane helical region and an *all-trans* retinal chromophore bound to the only lysine residue in helix G. The retinal and the lysine sidechain form a protonated Schiff base (pSB) as the primary binding site for the Cl^- ion. The inward Cl^- pumping function of HR is achieved with a cyclic conformational change called the photocycle which begins with the light-induced isomerization of retinal from *all-trans* to *13-cis* conformation.

Natronomonas pharaonis HR (*Np*HR) is one of the most extensively studied HRs because it can be functionally expressed with large amount in *E. coli* membrane [6] and is widely used as an optogenetics tool for silencing neurons [7]. The most adopted photocycle scheme for *Np*HR involves a series of kinetically distinguishable intermediates: *Np*HR + $h\nu \rightarrow K \rightarrow L_1 \rightarrow L_2 \rightarrow N \leftrightarrow O \rightarrow$ *Np*HR′ $\rightarrow$ *Np*HR, where N and O intermediates are in a quasi-equilibrium state, and absorption spectra of *Np*HR′ and *Np*HR are reported to be similar [8]. The two sub-intermediates for L, L_1 and L_2, also exhibit similar absorption spectra while the Cl^- ion location is different [9]. Subsequent studies have revealed that the Cl^- release takes place in the N → O step and Cl^- ion uptake from the extracellular medium takes place in the O → *Np*HR′ step [10,11]. Further spectroscopic studies on wild-type (WT) *Np*HR and its mutants have identified several key residues for the Cl^- transport process [11–21]. Numerous studies are reported for the earlier part of the photocycle, i.e., *Np*HR to the O intermediate based on the time-resolved

* Corresponding author at: Institute for Protein Research, Osaka University, 3-2 Yamadaoka, Suita, Osaka 565-0871, Japan.
E-mail address: yoh@protein.osaka-u.ac.jp (Y. Matsuki).

https://doi.org/10.1016/j.bpc.2024.107329
Received 31 July 2024; Received in revised form 21 September 2024; Accepted 22 September 2024
Available online 24 September 2024

crystallography experiments [9]. Together with the knowledge of the key residues, the Cl^- releasing mechanism and associated structural changes were elucidated. However, the Cl^- recapture process in the late photocycle remains unclear. The structural change from the O intermediate to the ground state was poorly characterized in crystal because the crystalline lattice packing prevented tracing the whole photocycle in crystal [9]. Even though crystal structures are available for *Np*HR both in the Cl^--bound ground state and an O-like anion-free state (referred to as the Cl^--bound and Cl^--free state, respectively) [22,23], where the latter Cl^--free state is assumed to represent the O intermediate because of their structural similarity [24,25]. Directly tracing the changes from the Cl^--free state to the Cl^--bound state failed because of the difficulty in achieving the Cl^- removal and recapture in crystal, where an M-like yellow form was required as an intermediate [23]. Also, although the photochemical studies under a high-pressure condition clearly suggested that there is a large molecular volume change between the O-intermediate and ground state [10,13], crystal structures showed changes only in the extracellular part of the helix C [23]. These results suggest that the physiological conformational change in the late photocycle is difficult to observe in crystal, leading to the paucity of direct structural insights into the Cl^- recapture process. For a better understanding of the Cl^- uptake process of *Np*HR and the associated structural changes between the Cl^--bound and -free states, atomic resolution study under a near-physiological condition is necessary.

Magic-angle spinning (MAS) solid-state nuclear magnetic resonance (ssNMR) spectroscopy is a promising method to this end, allowing atomic resolution molecular structural and dynamic studies of membrane proteins in near-physiological lipid bilayer conditions and ambient temperatures [26,27]. MAS ssNMR has been previously applied to opsin structural analysis of microbial rhodopsins [28–30] as well as for the high-precision structural studies on the Schiff bases [31–35].

In this study, we employed 3D ^{13}C-detection ssNMR spectroscopy to study structural differences of *Np*HR reconstituted in DMPC liposome between its Cl^--bound and -free states at ambient temperature. The structural differences were identified from the chemical shift perturbations (CSPs) in the ssNMR spectra. The identified key residues were mutated, and photochemical properties were analyzed further. We also used dynamic nuclear polarization (DNP) sensitivity-enhanced ssNMR technique for elucidating conformational distribution around pSB. Overall, the data suggested the large structural changes in the late photocycle, and allowed us to propose a model describing the Cl^- uptake process.

2. Materials and methods

2.1. Genes construction

A truncated wild-type *Np*HR (WT *Np*HR) with amino acids with the residue number from 18 to 277 was used for the measurement. The truncated *Np*HR gene was amplified from a *Np*HR gene coded in pET-21c (+) vector [19] with primers containing the *Nde*I or *Sal*I recognition sequences through the standard PCR method. The PCR products were digested using these restriction enzymes and then the fragments were ligated into NdeI and *Xho*I digested pET-22b(+) vector. Consequently, the WT *Np*HR with 6-His-tag at the C terminus was constructed, the final sequence was $ME^{18}VTQR\ldots VVSGS^{277}VEHHHHHH$. All *Np*HR mutants in this study were provided from this constructed vector through QuikChange™ method (Agilent).

2.2. Protein expression and purification

The *Np*HR was overexpressed in *E. coli* BL21(DE3) cells. For photochemical experiments, the natural abundance proteins were prepared using the LB media. For ssNMR experiments, the isotope-labeled proteins were prepared using the M9 minimal media. The uniformly ^{13}C- and ^{15}N-labeled WT *Np*HR sample, referred to as [U-^{13}C, ^{15}N]-*Np*HR, was prepared using [U-^{13}C] glucose and $^{15}NH_4Cl$ as the sole carbon and nitrogen sources, respectively. Sparsely ^{13}C-labeled and uniformly ^{15}N-labeled WT *Np*HR samples, referred to as [1,3-^{13}C, U-^{15}N]- and [2-^{13}C, U-^{15}N]-*Np*HR, were prepared using [1,3-^{13}C]- or [2-^{13}C]-labeled glycerol and $^{15}NH_4Cl$, respectively. $^{15}N_\zeta$-Lysine-labeled *Np*HR, referred to as [$^{15}N_\zeta$-Lys]-*Np*HR, was prepared by adding $^{15}N_\zeta$-Lys to natural abundance glucose and NH_4Cl based media. For [U-^{13}C, ^{15}N]-*Np*HR, 2 g of [U-^{13}C] glucose was used per liter culture, while for the sparsely ^{13}C-labeled samples, 3 g of the ^{13}C-labeled glycerol was used. For [$^{15}N_\zeta$-Lys]-*Np*HR, 100 mg of $^{15}N_\zeta$-Lysine was added when the optical density of culture at 660 nm (OD_{660}) reached 0.8. For these isotope-labeled *Np*HR samples, 1 g of either natural abundant or ^{15}N enriched NH_4Cl was used per liter culture.

The *E. coli* cells were grown at 37 °C by monitoring the growth by measuring the OD_{660}. The *Np*HR expression was induced by an addition of 1 mM isopropyl β-D-1-thiogalactopyranoside (IPTG) when OD_{660} reached 1.4. Simultaneously, 10 μM *all-trans* retinal was added to exogenously regenerate the expressed opsins. After 4 h of induction, the cells were harvested by centrifugation (4000 ×*g*, 10 min, 4 °C), then washed by 50 mM Tris-HCl (pH 8.0) with 5 mM $MgCl_2$ once and pelleted via centrifugation (4000 ×*g*, 10 min, 4 °C), stored at −20 °C.

The purification procedure was essentially the same as previously reported [36] with a slight modification. Briefly, the cells were resuspended using 50 mM Tris-HCl (pH 8.0) with 5 mM $MgCl_2$ and disrupted by ultrasonication. Then, the crude membranes were collected by ultracentrifugation (120,000 ×*g*, 60 min, 4 °C) and suspended using 50 mM Tris-HCl (pH 8.0) with 100 mM NaCl and 5 mM imidazole. The suspended membrane fraction was solubilized by an addition of 1.5 % n-dodecyl-β-D-maltoside (DDM) with stirring overnight at 4 °C. After solubilization, the insoluble part was removed by ultracentrifugation (120,000 ×*g*, 30 min, 4 °C). The supernatant containing *Np*HR was incubated with Ni-NTA resin (Qiagen) for 1 h at 4 °C, and then the resin was transferred to an empty chromatography column. Then the resin was washed by 50 mM Tris-HCl (pH 8.0) with 100 mM NaCl, 50 mM imidazole and 0.1 % DDM of 5-fold the resin volume to eliminate nonspecifically bound components. The purple fraction containing *Np*HR was collected by elution using 50 mM Tris-HCl (pH 8.0) with 100 mM NaCl, 500 mM imidazole and 0.1 % DDM.

2.3. Proteoliposome preparation

A PD-10 desalting column filled with Sephadex™ G-25 (Cytiva, referred to as PD-10 column) was used to remove the imidazole from the purified samples through exchanging against 50 mM Tris-HCl (pH 7.0) with 100 mM NaCl and 0.1 % DDM. After the buffer exchange, *Np*HR concentration was determined by the absorbance of opsin-bound retinal at 580 nm using the extinction coefficient, ε_{max} of 54,000 $M^{-1}\cdot cm^{-1}$ [37] for which we used an UV–vis spectrophotometer (SHIMADZU UV1280). 14:0 PC (DMPC) was dissolved with chloroform in a glass bottle then formed lipid film under dry N_2 or Ar gas flow by evaporating chloroform. The DMPC film was rehydrated with the *Np*HR solution and incubated for 1 h at 30 °C under gentle shake. The DDM was removed by incubating with bio-beads (Bio-Rad, 50 mg bio-beads for 1 mg DDM) overnight at 4 °C to form *Np*HR-DMPC proteoliposome. The proteoliposome was collected by centrifugation (18,000 ×*g*, 10 min, 4 °C) and annealed by a heat-chill cycle (7 min 30 °C water bath and 8 min ice bath) for 10 times then washed by 1 mL of 50 mM sodium acetate (pH 5.0) with 100 mM NaCl or 67 mM Na_2SO_4 for 5 times and resuspended in the same buffer to prepare Cl^--bound or Cl^--free *Np*HR samples, respectively. The Cl^- depletion for the Cl^--free *Np*HR ssNMR samples was checked with the change in the opsin bound retinal absorbance wavelength (λ_{max}) using the visible absorption spectra. The proteoliposome suspension was directly measured with the UV–vis spectrometer and the λ_{max} changes were analyzed.

2.4. ^{13}C detection MAS ssNMR spectroscopy and spectra analysis

The prepared proteoliposomes were packed into 3.2 mm Varian-style rotors with a home-made rotor packing tool via ultracentrifugation (100,000 ×*g*, 20 min, 4 °C) [38].

All ^{13}C detection ssNMR experiments were carried out on a 600 MHz (B_0 = 14.1 T) JEOL ECAII spectrometer with a Varian T3-HXY triple resonance probe. The MAS rate was set to 12.5 kHz or 14 kHz. A cooling gas was used to maintain the sample temperature to ~20 °C under MAS, as estimated using the temperature-dependent $K^{79}Br$ longitudinal relaxation time [39]. NCA [40], NCACX [41], NCOCX [41], CANCO [42], CANcoCA [43] and NcoCACX [44] spectra were recorded for [U-^{13}C, ^{15}N]-*Np*HR in the Cl^--bound state, while NCACX and CANCO spectra were also performed for [U-^{13}C, ^{15}N]-*Np*HR in the Cl^--free state. For [1,3-^{13}C, ^{15}N] and [2-^{13}C, ^{15}N]-*Np*HR, NCACX, NCOCX and CANCO experiments were recorded in the Cl^--bound state. The ^{13}C chemical shift was referenced to sodium 2,2-dimethyl- 2-silapentane-5-sulfonate (DSS) using the adamantane CH_2 peak at 40.48 ppm [45]. ^1H and ^{15}N chemical shift was indirectly referenced to DSS and liquid ammonia, respectively [46].

The NMR data were processed with NMRPipe [47]. NMRFAM-Sparky [48] and CcpNmr [49] were used for spectra visualization and analysis. The FLYA algorithm in CYANA software was used for the automated resonance assignment [50,51] to aid manual assignment procedure. The CYANA library file was adapted for the sparsely ^{13}C-labeled samples. The detailed parameters of the pulse sequences and data processing are given in supporting information.

2.5. Photochemical properties analysis

The purified *Np*HR was passed through the PD-10 column equilibrated with the buffer corresponding measuring conditions.

For the measurements of the Cl^- dependent absorbance change, Cl^--free *Np*HR samples were prepared in 50 mM PIPES (pH 7.0) and 0.1 % DDM. Then the UV–vis spectra were measured under various concentrations of NaCl from 0 to 1 M by adding 5 M NaCl. The Cl^- dependent absorption changes were analyzed using the Hill equation:

$$\Delta A_{\mathrm{rel.}} = \frac{[\mathrm{Cl}^-]^n}{K_{\mathrm{d}}^n + [\mathrm{Cl}^-]^n}. \quad (1)$$

where $\Delta A_{\mathrm{rel.}}$ is the normalized reduced absorbance at the wavelength where the difference spectra between Cl^--bound and -free state reached maximum, and n is the Hill-coefficient.

Circular dichroism (CD) spectra were measured using a JASCO J-1500 circular dichroism spectrophotometer at 25 °C. The *Np*HR samples were suspended first to 50 mM PIPES buffer (pH 7.0) and 0.1 % DDM with 100 mM NaCl. Then, the Cl^- concentration was reduced by mixing with appropriate volume of Cl^--free buffer 50 mM PIPES (pH 7.0) and 0.1 % DDM with 67 mM Na_2SO_4 and the protein was concentrated using ultrafiltration devices (Amicon® Ultra centrifugal filter 10 kDa cutoff, Sigma). All spectra were recorded in the region of 400–700 nm with a scanning speed of 20 nm/min 4 times. For the effect of the light-irradiation, samples were illuminated with a home-made LED array (12 × LEDs, 590 nm, total outpower ~10 W, OptoSupply) at 4 °C maintained by circulating water before the CD measurements.

For flash-photolysis measurement, the measuring medium was 50 mM PIPES (pH 7.0), 1 M NaCl and 0.1 % DDM, while the *Np*HR concentration was adjusted to $Abs_{max} \approx 0.5$ by concentration using ultrafiltration devices (Amicon® Ultra centrifugal filter 10 kDa cutoff, Sigma). The flash photolysis apparatus was described previously [52]. A Nd-YAG laser (532 nm, 7 ns) was used for exciting *Np*HRs, for each measured wavelength (400–700 nm, at 10 nm intervals) 60 laser pulses were used to improve the S/N ratio. The data were analyzed with a 4-pigments irreversible sequential model [18,53]:

$$P_0 \rightarrow P_1 \xrightarrow{\tau_1} P_2 \xrightarrow{\tau_2} P_3 \xrightarrow{\tau_3} P_4 \xrightarrow{\tau_4} P_0.$$

where, P_0 is the ground state before the light irradiation. P_i is the kinetically defined intermediates in the photocycle and τ_i is the corresponding time constant (i = 0 – 4). The observed photolysis data were globally fitted to calculate the time constants and absorption spectrum of each intermediate using scripts in Python3 written in-house with NumPy and SciPy packages.

2.6. Size-exclusion chromatography (SEC)

SEC was conducted using a Superdex™ 200 Increase 10/300 GL column with AKTA pure™ 25 M1 system (Cytiva). The *Np*HR samples for SEC were suspended to 10 mM PIPES buffer (pH 7.0) with 0.1 % DDM and 100 mM NaCl or 67 mM Na_2SO_4 for Cl^--bound or -free samples, respectively. 200 μL samples containing ~27 μM *Np*HR (Abs_{580} = 1.5) were applied to the column pre-equilibrated with the same buffer. The flow rate was 0.75 mL/min and the eluted *Np*HRs were detected by the absorption at 580 nm.

2.7. Ultra-low temperature DNP MAS ssNMR spectroscopy and spectral analysis

The proteoliposomes that contain [$^{15}N_\zeta$-Lys]-*Np*HR in the Cl^--bound and -free states were washed once with 100 μL aliquot of deuterated "DNP juice", which is the mixture in 1:3:6 ratio of the buffer: D_2O: glycerol-d_8 (*v*/v/v). As a DNP polarizing agent, biradical compound AMUPoL [54] was used. The buffer solution contained 200 mM AMUPoL, 500 mM sodium acetate with 1 M NaCl or 670 mM Na_2SO_4 (pH 5.0), so that the final concentration becomes 20 mM AMUPoL, 50 mM sodium acetate with 100 mM NaCl or 67 mM Na_2SO_4 (pH 5.0) to ensure the ion concentration in the sample. The suspended sample in the DNP juice was well vortexed and centrifuged to remove extra DNP juice, then packed into a JEOL Si_3N_4 3.2 mm rotor using a home-made packing tool under centrifugation (2000 ×*g*, 15 min). One of the rotor spacers was hollowed to contain $K^{79}Br$ powder for the temperature measurement.

The DNP MAS ssNMR experiments were carried out on a 700 MHz (B_0 = 16.4 T) JEOL ECAII spectrometer, equipped with a dedicated triple-resonance DNP MAS NMR probe, the custom-built closed-cycle helium gas sample spinning system [55] and a 460 GHz gyrotron (output power ~ 10 W) for generating microwaves. The probe was cooled with helium gas to 30 K and MAS frequency was set to ~7.5 kHz, while the sample temperature under MW irradiation was estimated to be 35 K using $K^{79}Br$ [39]. The data were processed and analyzed with the JEOL Delta software. The detailed parameters of the pulse sequences and data processing are described in supporting information.

3. Results

3.1. Liposome preparation

The protein-to-lipid (P/L) ratio for the proteoliposome sample was optimized to obtain the best ssNMR spectral quality. The [U-^{13}C, ^{15}N]-*Np*HR to DMPC molar ratios ($n_{NpHR} : n_{DMPC}$) of 1:15, 1:10 and 1:5 were evaluated. These correspond to the weight ratios ($w_{NpHR} : w_{DMPC}$) of 3:1, 4:1 and 9:1, respectively. 2D-NCA correlation spectrum was measured for each condition as shown in Fig. S1. Observed signal linewidths (~100 Hz for ^{13}C and ~150 Hz for ^{15}N) were similar in all conditions. Also, the chemical shifts were not affected by the P/L ratio. These results suggest homogeneous *Np*HR-DMPC proteoliposome was formed even with the highest P/L ratio. The sensitivity improvement observed for the highest (9:1, *w*/*w*) versus the lowest (3:1) P/L ratio samples was 1.2-fold, which was consistent with the corresponding fractional weight ratio for protein ($w_{NpHR} : w_{NpHR} + w_{DMPC}$) of 0.9 versus 0.75, respectively, assuming the same density for protein and lipid bilayer portions.

To confirm the high P/L ratio does not affect the Cl^- binding affinity of *Np*HR, visible absorption spectra were recorded for the reconstituted samples with and without Cl^-. Note that Cl^- ion can be easily removed from *Np*HR in the native membrane by buffer exchange, while the Cl^- depletion from *Np*HR crystal requires soaking in basic solution (pH 9.3) because of the lattice force [23]. The λ_{max} values observed for the 1:5-P/L ratio sample before and after washing with a Cl^--free buffer (50 mM sodium acetate, pH 5.0 with 67 mM Na_2SO_4) was 579 nm and 595 nm, respectively (Fig. S2). These values were identical to the literature values reported for *Np*HR in the Cl^--bound and -free states [15]. This result shows the Cl^- ions can be depleted completely from *Np*HR in DMPC liposome and that the liposome with the 1:5 P/L ratio provides a valid near-physiological condition suitable for the structural analysis. Thus, we use the P/L ratio of 1:5 for all the following experiments.

3.2. Chemical shift assignment

MAS ssNMR measurements were performed first for the [U-^{13}C, ^{15}N]-*Np*HR in the Cl^--bound state. A CANCO spectrum, which virtually provides one signal per residue, was used to evaluate the sample quality. We found ~140 peaks in the CANCO spectrum, while the number of residues for [U-^{13}C, ^{15}N]-*Np*HR is 269. The insufficient number of signals can be due to the signal overlap or poor magnetization transfer efficiency for mobile molecular regions.

Chemical shift assignment was performed by combining the CANCO, NCACX, NCOCX, CANcoCA and NcoCACX data. However, the complete/unambiguous assignment was still difficult because of severe signal overlaps and partly missing side chain signals. Thus, additional NCACX and NCOCX spectra were recorded for [1,3-^{13}C, U-^{15}N]- and [2-^{13}C, U-^{15}N]-*Np*HR, prepared using [1,3-^{13}C]- and [2-^{13}C]-glycerol as the sole carbon source of *E. coli* culture. This sparse ^{13}C labeling reduced the total number of peaks while the specific labeling pattern helped to recognize residue types [56]. The sparse ^{13}C labeling also reduced the signal linewidths by removing the homonuclear one-bond ^{13}C scalar couplings and mitigated the signal overlap [56,57]. This increased the number of unambiguous assignments for *Np*HR (Fig. S3).

The obtained data were analyzed using automatic assignment algorithm FLYA and results were used to aid the manual assignment. The data from sparsely ^{13}C-labeled samples could not be analyzed well with the FLYA assignment tool, and required modifications on the descriptions of atoms and experiments in the library files. An example of the sequential assignment using spectra of [U-^{13}C, ^{15}N]-*Np*HR are shown in Fig. 1. Total 27 backbone nitrogen, 32 C_α and 30 C' signals (25 N_H- C_α-C' intra-residue pairs) were assigned in a major part of helix D, C-D loop and E-F loop on the cytoplasmic side and the nearby helical residues, together with a few residues in the other helices. The assigned chemical shifts are tabulated in Table S6. Other nuclei were not assigned without ambiguity because of the amino acid type degeneration and signal losses in the flexible regions.

3.3. Structural changes by Cl^- depletion

Next, NCACX, NCOCX and CANCO spectra were recorded for [U-^{13}C, ^{15}N]-*Np*HR in the O-like Cl^--free state to evaluate the structural changes upon Cl^- depletion. Similar assignment strategy for the Cl^--bound state was used for the Cl^--free state *Np*HR as well. The assignment results of the Cl^--free state *Np*HR are tabulated in Table S7. Smaller number of signals (~120 peaks) were found for the Cl^--free state *Np*HR than for the Cl^--bound state, presumably due to the increased molecular mobility in the Cl^--free state. We have identified in the CANCO spectra ~100 peak pairs between the Cl^--bound and -free state (Fig. 2a-c). The chemical shift perturbations (CSPs) for these peak pairs were calculated using the backbone $^{15}N_H$ and $^{13}C_\alpha$ shifts, δN_H and δC_α, as:

$$\Delta\delta = \sqrt{(\delta C_{\alpha,\ \text{with Cl}^-} - \delta C_{\alpha,\ \text{without Cl}^-})^2 + 0.4(\delta N_{H,\ \text{with Cl}^-} - \delta N_{H,\ \text{without Cl}^-})^2}. \quad (2)$$

The average CSP was $\overline{\Delta\delta} = 0.22$ ppm for all the peak pairs, while only 30 % of them exhibited CSPs larger than 0.275 ppm, which we refer to as the top 30th percentile threshold, $\Delta\delta_{30th}$ (Fig. 2d). This result suggests that a major part of the protein experiences at least some conformational perturbation upon Cl^- depletion, while a smaller subset of the amino acid residues experiences much more significant conformational change. Below, we examine CSPs for the assigned residues for more residue-specific discussion.

CSPs for assigned residues are summarized in Fig. 2e. A few resides in

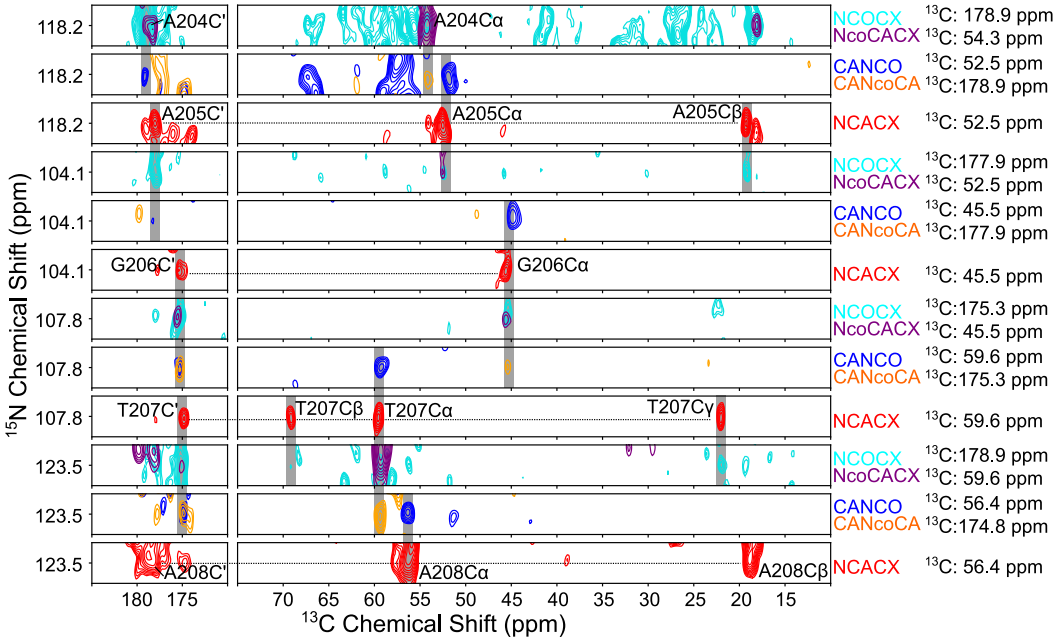

Fig. 1. An example of the "backbone walk" from A205 to A208 with the set of 3D spectra, shown for the Cl^--bound state [U-^{13}C, ^{15}N]-*Np*HR. The experiment names and chemical shifts for the 3rd axis are shown on the right of each plane. (For interpretation of the references to colour in this figure legend, the reader is referred to the web version of this article.)

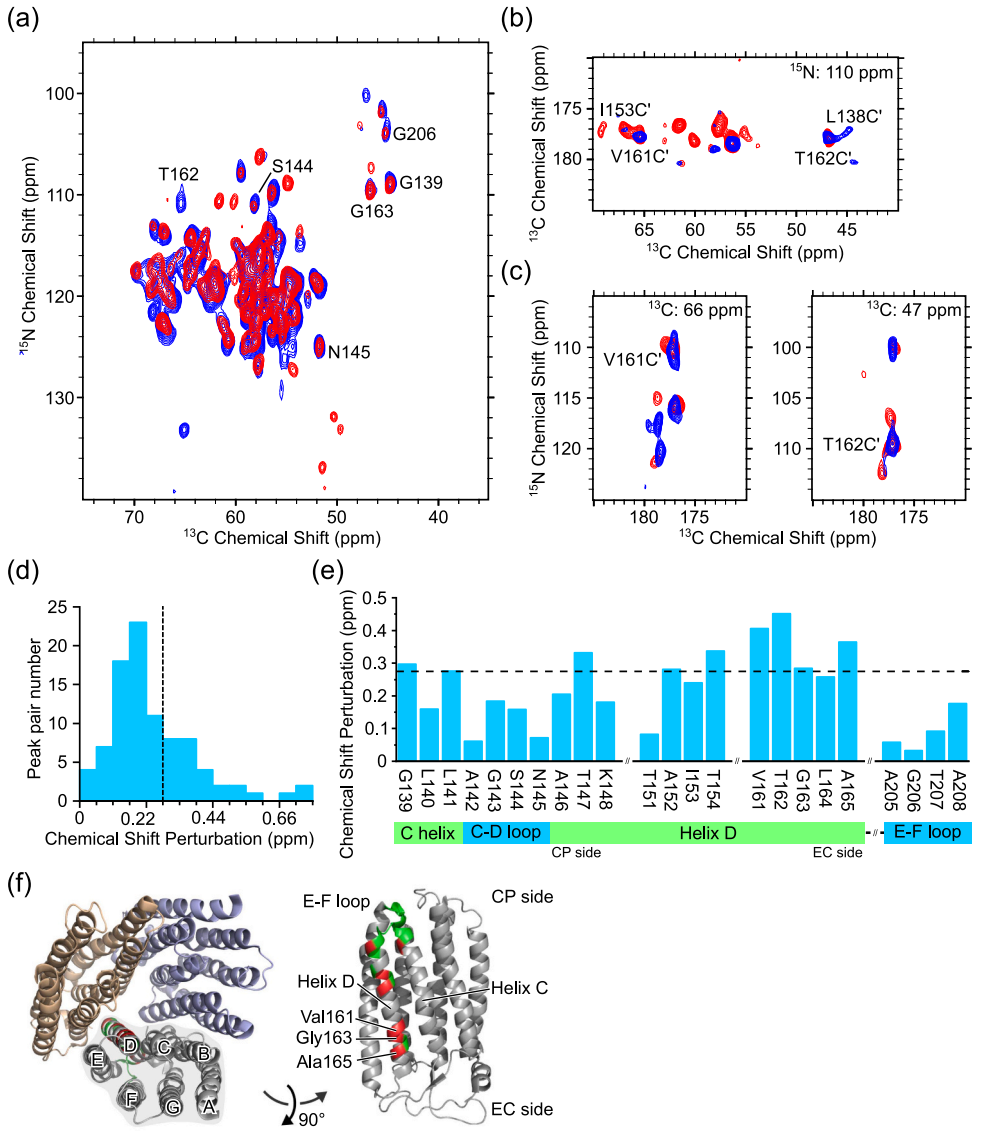

Fig. 2. (a) The 2D projection of 3D CANCO spectra recorded with [U-^{13}C,^{15}N]-*Np*HR in the Cl^--bound state (red) and -free state (blue). (b) A 2D C-C plane taken at δN_H = 110 ppm. (c) 2D C′-N planes taken at δC_α indicated in the upper conner. Assigned peaks are labeled. (d) Histogram of the number of peak pairs (N, C_α, C) in function of the CSP calculated by Eq. (2). The CSP value of $\Delta\delta_{30th}$ = 0.275 ppm is indicated by the dash line, which is the top 30th percentile CSP. (e) CSPs observed for the assigned peaks. The horizontal line indicates $\Delta\delta_{30th}$. (f) The *Np*HR structure (PDB entry: 3A7K [22]); assigned residues are colored (red for $\Delta\delta > \Delta\delta_{30th}$; green otherwise). Val161, Gly163 and Ala165 are labeled. The structure is visualized using PyMOL. (For interpretation of the references to colour in this figure legend, the reader is referred to the web version of this article.)

the cytoplasmic side of the helix C and D (Gly139-Thr154) showed significant CSPs, but the average CSP among this region (~0.19 ppm) was lower than $\Delta\delta_{30th}$. These residues are close to the Cl^- releasing channel in the cytoplasmic side [9]. Photochemical studies of the intermediates previously suggested structural changes arising for O formation remained until *Np*HR′ formation [11], and the N and O intermediates are under a structural quasi-equilibrium [8,53,58]. Therefore, the observed CSPs in the cytoplasmic side may be related to the Cl^- release process. The extracellular (EC) side of the helix D showed much larger CSPs: a stretch of five residues, Val161-Ala165, showed CSPs very close to or greater than $\Delta\delta_{30th}$ (the average CSP was ~0.35 ppm). This suggested that at least one of the major structural changes in *Np*HR occurred in the EC side of the helix D upon ion depletion. Importantly, in the X-ray structures, conformational change around the EC side of helix D was not observed, while finite changes were seen only for a part of helix C and B-C loop on the EC side [23]. We also note the EC part of helix D is adjacent to several residues important for Cl^- uptake such as His100, Arg176 and Glu234 [22]. Together, these data suggested the possibility that the EC side of the helix D plays a role in the Cl^- uptake process. To test and discuss this working hypothesis, we set out to the mutation study and additional spectroscopic analysis described below.

3.4. Molecular properties of NpHR mutants in helix D at extracellular part

We successfully expressed, purified and reconstituted the following mutants of *Np*HR: V161A, G163A and A165V (Fig. S4). The Cl^- dependent changes in absorption spectrum are shown for each mutant in Fig. 3. Fig. 3e plots the Cl^- concentration-dependent absorbance changes (Fig. S5) and their fit using the Hill equation (Eq. (1)), evaluating the Cl^- dissociation constants (K_d). The wavelengths of the opsin-bound retinal absorption peak (λ_{max}), K_d and the Hill coefficient are summarized in Table 1. For G163A mutant, we observed ~17 nm and ~20 nm blue-shift relative to WT for the Cl^--bound and -free state, respectively. For A165V mutant, no shift was observed for the Cl^--

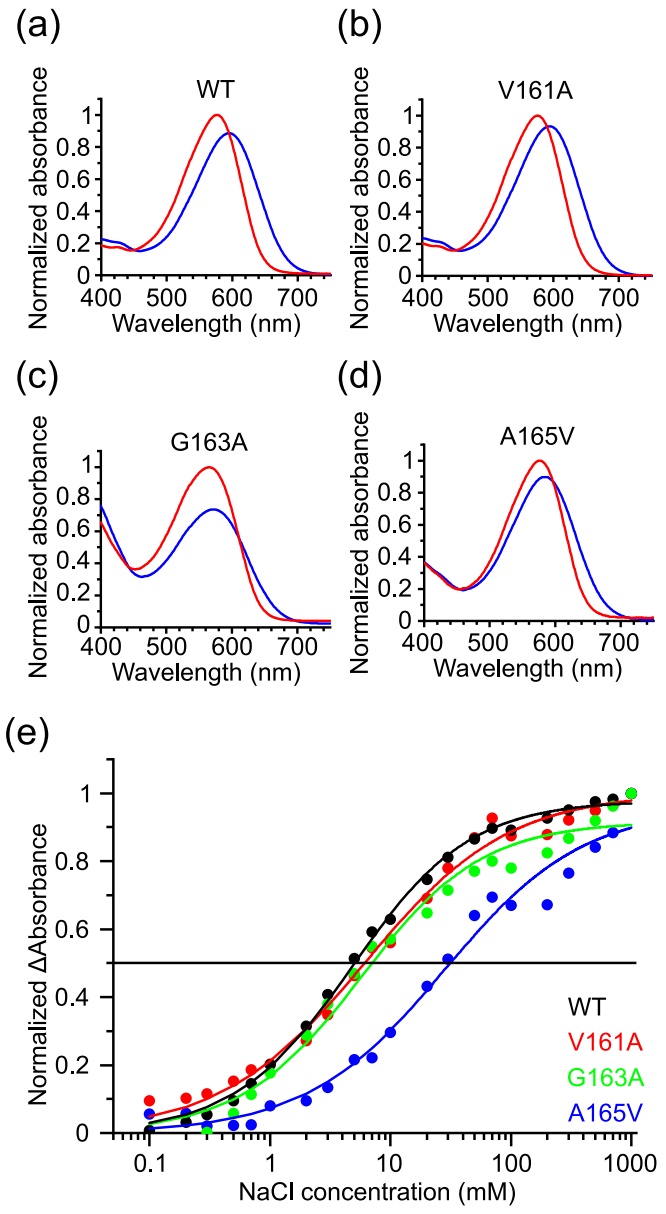

Fig. 3. Cl^- concentration-dependent absorption change observed for *Np*HR in wild type and mutants. (a-d) UV–vis spectra recorded with Cl^--bound (100 mM Cl^-, red) and -free (blue) state WT *Np*HR, V161A, G163A and A165V mutants, respectively. (e) Change of the absorption maximum versus Cl^- concentration. Each curve is normalized by the maximum positive change. The solid curves show the best-fit results using the Hill equation (Eq. (1)). (For interpretation of the references to colour in this figure legend, the reader is referred to the web version of this article.)

Table 1
Absorption maxima (λ_{max}), Cl^- dissociation constants (K_d), Hill coefficients (n) for solubilized WT *Np*HR and the mutants in 0.1 % DDM at pH 7.0.

Opsin type	λ_{max} / nm		K_d / mM	n
	Cl^- free	100 mM NaCl		
WT	595	577	4.8	0.89
V161A	595	576	6.1	0.73
G163A	575	560	5.7	0.87
A165V	584	576	28	0.75

bound state, while ~10 nm blue-shift was observed for the Cl^--free state. This latter observation was also reported for F150A, F150W and F150Y mutants that destabilized the physiological trimeric assembly of *Np*HR [59]. It is also to be noted that A165V mutant was the only mutant that exhibited a significant increase in K_d among the tested mutants.

Next, flash laser-induced transient absorption changes were measured for WT and the mutants with 1 M NaCl (Fig. 4), and analyzed using the model described in Materials and Methods. The extracted time constants τ_i ($i = 1 - 4$) are summarized in Table 2. Calculated absorption spectrum for the intermediates P_i are shown in Fig. S6. For P_1 and P_2, the retinal absorption peaks were both blue shifted to λ_{max} ~520 nm. Therefore, they are identified as the L_1 and L_2 intermediates. Consistently, P_3 showed the typical double-peak absorption and is identified as the N-O quasi-equilibrium. P_4 exhibited similar absorption spectra to the ground state and is identified as the *Np*HR′ state. The photocycle of V161A was almost identical to WT, while those for G163A and A165V were distinct. The smaller peak of the differential absorption (Δ_{abs}) at 650 nm found in the late photocycle (~1 ms) for G163A and A165V (Fig. 4c, d) suggests a reduced formation of the O intermediate; this was consistent with the only minor peak seen around 600 nm in P_3 absorption spectra (Fig. S6c, d). Moreover, G163A and A165V mutant showed, respectively, much slower (Fig. 4c) and faster recovery of Δ_{abs} at 580 nm (Fig. 4d), i.e., significantly longer or shorter (τ_3, τ_4) than WT, respectively. Altogether, these observations indicate the mutations in the EC side of helix D perturb the late photocycle indeed, including the Cl^- release/uptake steps. Interestingly, τ_4 of A165V was ~5 times shorter than that for WT and close to that reported for the F150A mutant. The F150A mutant was reported to have the unstable trimeric assembly, which resulted in the faster photocycle while inefficient ion pumping [59].

Intrigued by the similarity of the photochemical properties between the A165V and F150A mutants, we tested the trimer integrity of the A165V mutant using SEC (Fig. 5) and visible CD spectroscopy (Fig. S7) [59]. The A165V mutant was found to be in the trimeric form in presence of 100 mM NaCl with 0.1 % DDM while the dissociation was observed upon removal of Cl^- ion through buffer exchange. To check whether this trimer dissociation is reversible, we collected the A165V monomer fraction (elution volume of 12–15 mL), back-exchanged to the Cl^--containing (100 mM) buffer and applied to SEC again after concentration (Fig. 5b, black line). The elution pattern remained identical, i.e., the A165V trimer dissociation is irreversible. For WT *Np*HR as well as the V161A and G163A mutants, the trimer formation was not affected by the Cl^- depletion (Figs. 5a and S7a-c). This indicates that the bulky valine sidechain in the A165V mutant located at the monomer-monomer interface uniquely causes the trimer dissociation. We also confirmed that the A165V trimer dissociates under the Cl^--existing, light illumination condition, i.e., during the photocycle, while WT *Np*HR trimer does not (Fig. 6). The A165V mutant formed the same trimeric structure as WT in the Cl^--bound state in dark, thus the dissociation is not simply due to the bulky valine sidechain. From these results, we hypothesized that the EC part of helix D significantly moves outward in the late photocycle, which may be crucial for the Cl^- uptake process. This possibility will be further discussed in Discussion section.

3.5. Environmental changes of protonated Schiff Base induced by the mutations

The above spectroscopic data showed the chromophore absorption wavelength is affected by the mutation in helix D. In general, the chromophore absorption wavelength of microbial rhodopsins is sensitive to the environment around the protonated Schiff base (pSB). To gain more insight into the conformational states around pSB, we measured the pSB ^{15}N NMR for *Np*HRs (N_ζ of Lys256) using the DNP-enhanced ssNMR technique. The DNP-enhanced ssNMR was previously used for structural analysis of retinal with a sub-angstrom resolution which are impossible without DNP [60–62]. In our case, as shown below, the

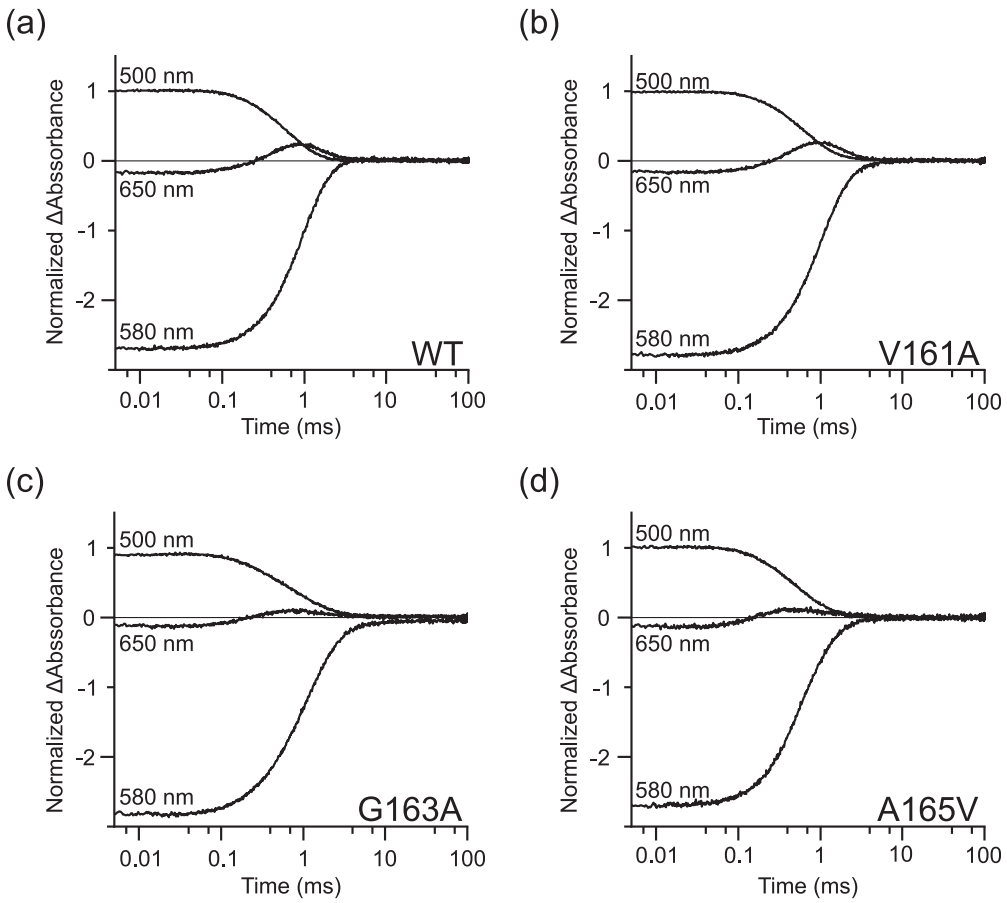

Fig. 4. Photocycle of *Np*HR in wild type and mutants. (a-d) Flash-induced transient absorption measured at indicated wavelengths is plotted as a function of time for WT *Np*HR, V161A, G163A and A165V mutants, respectively.

Table 2
Time constants for the formation of each intermediate extracted from the flash photolysis data using the sequential irreversible model.

Opsin type	τ_1 / ms	τ_2 / ms	τ_3 / ms	τ_4 / ms
	$L_1 \rightarrow L_2$	$L_2 \rightarrow$ N-O	N-O $\rightarrow$ *Np*HR′	*Np*HR′ $\rightarrow$ *Np*HR
WT	0.228	0.307	0.792	34.283
V161A	0.167	0.395	0.866	30.169
G163A	0.043	0.324	1.085	64.500
A165V	0.101	0.111	0.556	6.500

increased sensitivity allowed us to identify, for the first time, multiple substates for the O-like Cl^--free state *Np*HR.

One-dimensional DNP-enhanced ^{15}N spectra of [$^{15}N_\zeta$-Lys]-WT and G163A and A165V mutants are shown in Fig. 7. The signal enhancement factor ε was ~30 at T ~30 K for all samples. This corresponds to a roughly 300-fold sensitivity gain together with the effect from the sample cooling relative to the conventional room-temperature ssNMR. This sensitivity allowed us to detect weak ^{15}N signals from minor conformations within hours. The ultra-low temperature DNP condition freeze-traps dynamical conformational ensembles thermally sampled by *Np*HR. Therefore, metastable conformational substates around pSB can be detected as ^{15}N peaks with distinct chemical shifts, where the linewidth and integral intensity of each peak reflects the degree of conformation disorder and population of each substate, respectively. The pSBs in Cl^--bound WT and A165V exhibited a single ^{15}N peak at ~162 ppm, while that of G163A showed split peaks at ~160, ~168 and ~180 ppm (indicated by dash lines in Fig. 7b), corresponding to three major conformational substates around the chromophore. The peak at ~168 ppm was highest in intensity while that at ~160 ppm seen also for WT and A165V mutant became much smaller. This data shows that the pSB environment for G163A is significantly different from that for WT and A165V mutant in the Cl^--bound state. Then, the same measurements were carried out for *Np*HRs in the Cl^--free state (Fig. 7c). The similar three substates were observed for all three samples. Again, spectra of WT and A165A were similar: the peak at ~162 ppm remained major with additional minor peaks seen at ~168 ppm and ~180 ppm. For the G163A mutant, the broad peak at ~180 ppm, corresponding to highly disordered substate, became highest in intensity while that at ~160 ppm much smaller. To summarize, we found for the first time that the O-like Cl^--free intermediate generally comprises three substates, and that the conformational setting for WT and A165V mutant are similar to each other, while G163A mutant is distinct with significantly more disordered conformation, perhaps a destabilized opsin fold.

The ^{15}N chemical shifts of pSB of many microbial rhodopsins follow an empirical linear relationship between $1/\lambda_{max}$ and $1/d^2$. Here, d is the distance between the pSB ^{15}N atom and the counterion [35,63–65] which is Cl^- for *Np*HR. In Fig. 7d, we plotted the pSB ^{15}N chemical shifts we observed for *Np*HRs versus $1/\lambda_{max}$. For WT (blue) and A165V (red), the ^{15}N shift closely followed the linear trend. The major ^{15}N peak (at ~168 ppm) observed for G163A mutant (green square) also followed the trend. In contrast, the ^{15}N peaks for the two minor substates (small green squares) wildly deviated from the relationship, suggesting a lot looser coordination of the counter ion. Overall, our data indicate that G163A mutation increases the population of the hidden substates that were not observed with WT, and that these highly disordered substates have much looser ion coordination geometry. This presumably resulted into the above observed long τ_3 and τ_4. For A165V, the structural environment around pSB was suggested to be similar to WT, and the abnormally

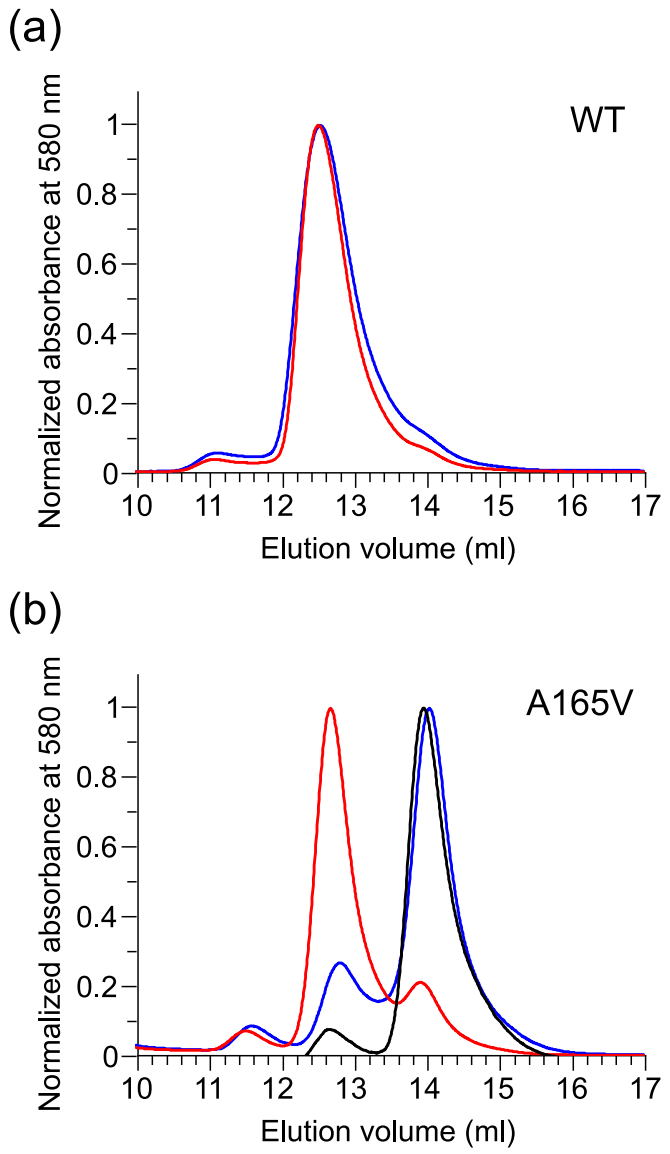

Fig. 5. Size-exclusion chromatograms recorded for WT *Np*HR (a) and A165V mutant (b) in Cl^--bound (red) and -free (blue) state. The black line shows data taken after the buffer exchange with the A165V mutant as described in the text. The *Np*HR elution peaks at 12.6 mL and 14.2 mL corresponds to the trimeric and monomeric form, respectively [59]. The small lead peak around 11–12 mL is from *Np*HR multimers. (For interpretation of the references to colour in this figure legend, the reader is referred to the web version of this article.)

short τ_3 and τ_4 should be attributed to some other determining factor, maybe the trimer dissociation.

4. Discussion

In this study, we performed ssNMR analysis on *Np*HR reconstituted in DMPC liposomes to study structural changes in the Cl^- release/uptake process. Then, we extended the study with amino acid mutations to the residues that exhibited large CSP. The photochemical properties and the pSB geometry of these mutants were analyzed. The Cl^--free state is known as the mimic of the O-intermediate that occurs just before the Cl^- uptake step. Therefore, we performed these analyses both in the Cl^--bound and -free state and compared. In the ssNMR analysis, structural changes in the EC part of helix D were suggested in comparing ^{15}N and ^{13}C chemical shifts between the Cl^--bound and -free state. To test the importance of this region in the ion uptake process, the photochemical properties and the pSB geometry were investigated using the point mutants of *Np*HRs: G163A and A165V. We found these mutations indeed significantly changes the molecular properties including the transition rates, populations between/of the photocycle intermediates as well as the pSB geometry.

Interestingly, we found that the A165V mutation destabilizes the trimeric structure in a low Cl^- concentration condition, and also over the course of the light-driven photocycles under a physiological Cl^- concentration. This trimer disruption may account for the observed abnormally short τ_4, which was also observed in the previous report on the trimer disrupted form of F150A mutant [59]. It should be noted that A165V mutant exhibited the same λ_{max} and pSB ^{15}N chemical shift with WT in the Cl^--bound trimeric state, which indicates that the whole opsin structure and that around the chromophore is not perturbed in the A165V mutant relative to WT in the ground state. Thus, the trimer destabilization is not because of a loose packing of monomer in general but related with some specific structural changes during O-intermediate or O-like Cl^--free state formation (Fig. 8a, b). The X-ray structural studies showed the Tyr124 sidechain rotates toward the helix D by Cl^- depletion, which is close to the 165th position. This rotation may push the EC part of helix D toward the adjacent monomer. The A165V mutant, which has a bulky sidechain at the monomer-monomer interface, may have been particularly affected by such structural transition and disturbed the trimer integrity (Fig. 8c, d). These observations strongly suggestes an outward movement of the EC part of helix D in the late photocycle including the O-intermediate.

The pSB chemical shift data were consistent with the hypothesized outward movement of helix D. In WT and A165V, the pSB ^{15}N peak was split into broad multiple peaks in the Cl^--free O-like state, suggesting coexistence of disordered substates with a looser packing around the retinal. The G163A mutant showed the blue-shifted λ_{max} and the similar pSB peak splitting even in the Cl^--bound state. This latter ^{15}N peak splitting was very similar to that with WT and A165V mutant in Cl^--free state, suggesting such loosened structure exist for G163A even in the Cl^--bound state. Gly163, known as a colour tuner, is highly conserved among rhodopsin family. Mutation in this residue was predicted to result in a blue shift of λ_{max} [67] because of the bulky sidechain here pushes the retinal β-ionone ring and distorts the polyene chain [68]. Therefore, this steric crush may have loosened the retinal packing in G163A in the Cl^--bound state. Importantly, in the Cl^--free state of G163A mutant, the ion depletion further significantly increased the intensity of the most downfield broad ^{15}N peak at ~180 ppm. This is consistent with the hypothesized outward movement of helix D that further reduces the retinal packing, exacerbating the disorder around pSB. Also, this loose and disordered molecular packing may account for the particularly long τ_3 and τ_4 observed for G163A mutant.

Based on the above discussion, we propose a model for the Cl^- uptake process comprising a movement of the EC side of the helix D as a crucial step for the ion uptake (Fig. 9). It has been reported that His100 in B-C loop, Arg123 in helix C, Arg176 in D-E loop and Glu234 in F-G loop together with the nearby water molecules forms a putative Cl^- uptake pathway [22]. Indeed, some open space between helices (colored cyan in Fig. 9a) can be found around these residues in the crystal structure of the O-like Cl^--free blue form. However, these residues are covered by the B-C loop and there is no obvious ion entrance path toward this space. The His100, Arg176 and Glu234 are clustered near the EC part of helix D, meanwhile helix D is not tightly covered by B-C loop. Therefore, an outward movement of helix D may be helpful to create a path for the Cl^- entrance. The Glu234 [12] in F-G loop and Tyr124 [22] in helix C are known as key residues for Cl^- transport and showed sidechain rotation between Cl^--bound and -free state. These movements together with the outward movement of the EC part of the helix D can allow Cl^- ion to enter the inner protein space and captured, which is further transported to the pSB region.

Still, some major points remain to be clarified. Although the mutations in helix D, such as A165V, F150A, F150 W etc. showed similar

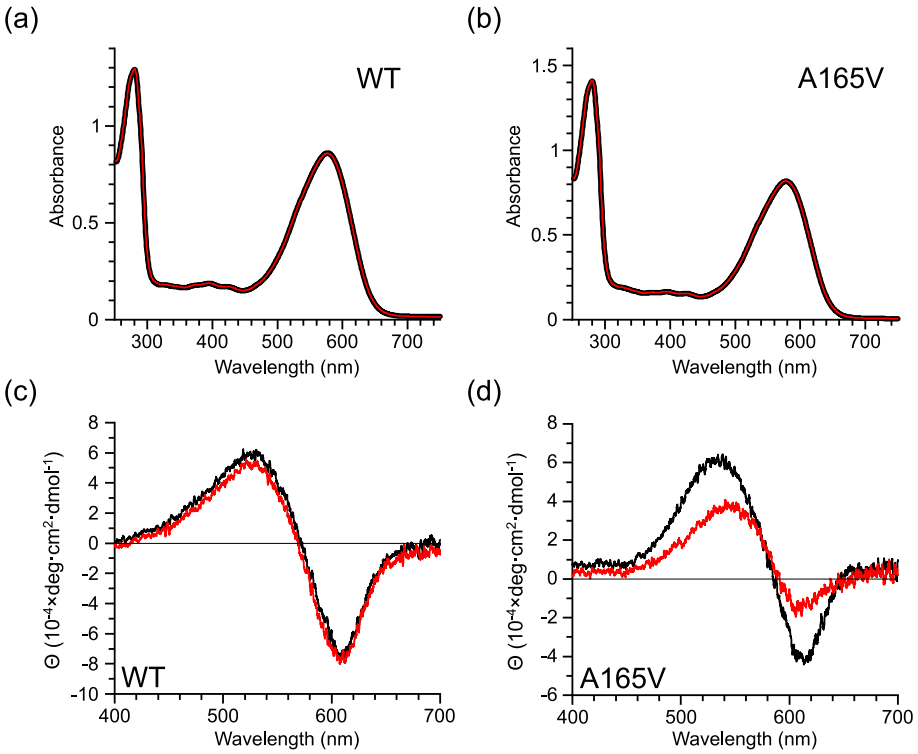

Fig. 6. The light-induced trimer dissociation of A165V mutant. UV–vis (a,b) and visible CD (c,d) spectra recorded for WT and A165V *Np*HR, respectively, before (black) and after (red) 15 h of illumination under 590 nm. The UV–vis spectra shows the illumination does not cause bleaching. After illumination, a change in the typical bi-polar CD couplet was observed for A165V mutant (d): the intensity of the red-shifted negative peak diminished, and the blue-shifted positive peak shifted toward λ_{max}, indicating the trimer dissociation for A165V mutant. (For interpretation of the references to colour in this figure legend, the reader is referred to the web version of this article.)

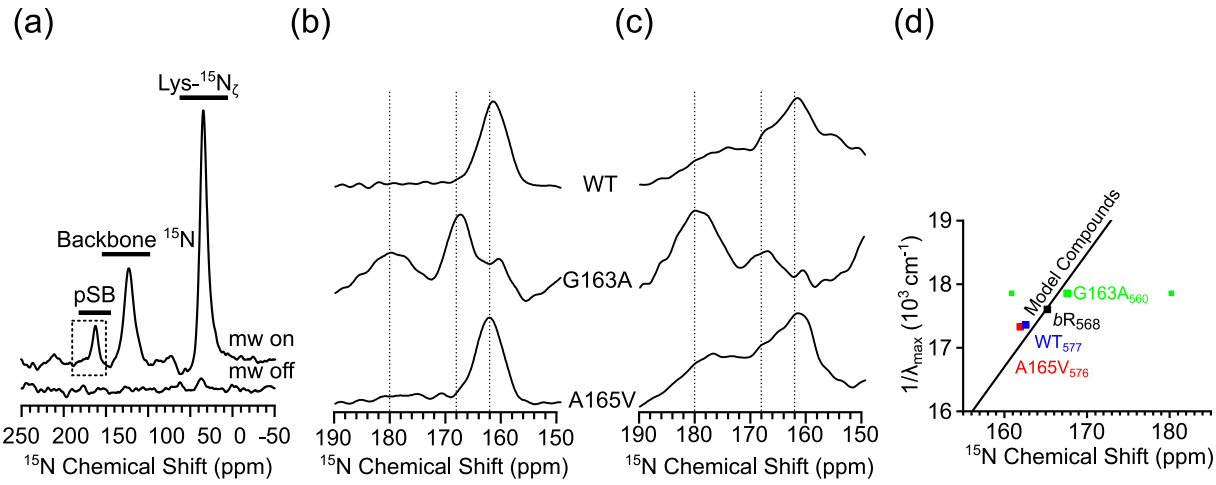

Fig. 7. ^{15}N NMR analysis for [$^{15}N_\zeta$-Lys]-*Np*HR WT and mutants. (a) Full NMR spectrum recorded for WT *Np*HR in the Cl^--bound state with and without the microwave irradiation for DNP. The pSB region blown up in (b,c) is indicated with a dashed rectangle. (b, c) Blowups of the pSB region of the CP-based DNP-enhanced ^{15}N spectra recorded for *Np*HRs in Cl^--bound (b) and -free state (c). (d) The linear relationship between $1/\lambda_{max}$ and the pSB ^{15}N chemical shift typically observed for the counterion-bound retinal derivatives. Data taken with *Np*HR WT, A165V and G163A mutants are shown in blue, red and green, respectively. The two smaller green squares correspond to the two minor ^{15}N peaks observed for G163A. Data for the model compounds and bR_{568} are adopted from Hu et al. [63] (For interpretation of the references to colour in this figure legend, the reader is referred to the web version of this article.)

properties such as the trimer disruption and abnormally short τ_4, K_d for the Cl^- binding observed for the A165V mutant was significantly larger than that for the Phe150 mutants. Also, λ_{max} for the A165V mutant red shifted upon Cl^- ion release, while that for the Phe150 mutants blue-shifted [59]. This suggests that A165V mutant in its O-like Cl^--free state has distinct conformation (distribution) to the that for Phe150 mutants, and more detailed structural analysis is in order to gain deeper insights into the Cl^- uptake process. The origin of the less accumulated O-intermediate in the N-O quasi-equilibrium observed for the G163A and A165V mutants than WT also remains unclear. The A165V mutant that shares some photochemical properties including the less accumulated O-intermediate with the F150A mutant may have the branched photocycle found previously for the F150A mutant [59]. On the other hand, the G163A mutant does not share such properties with known

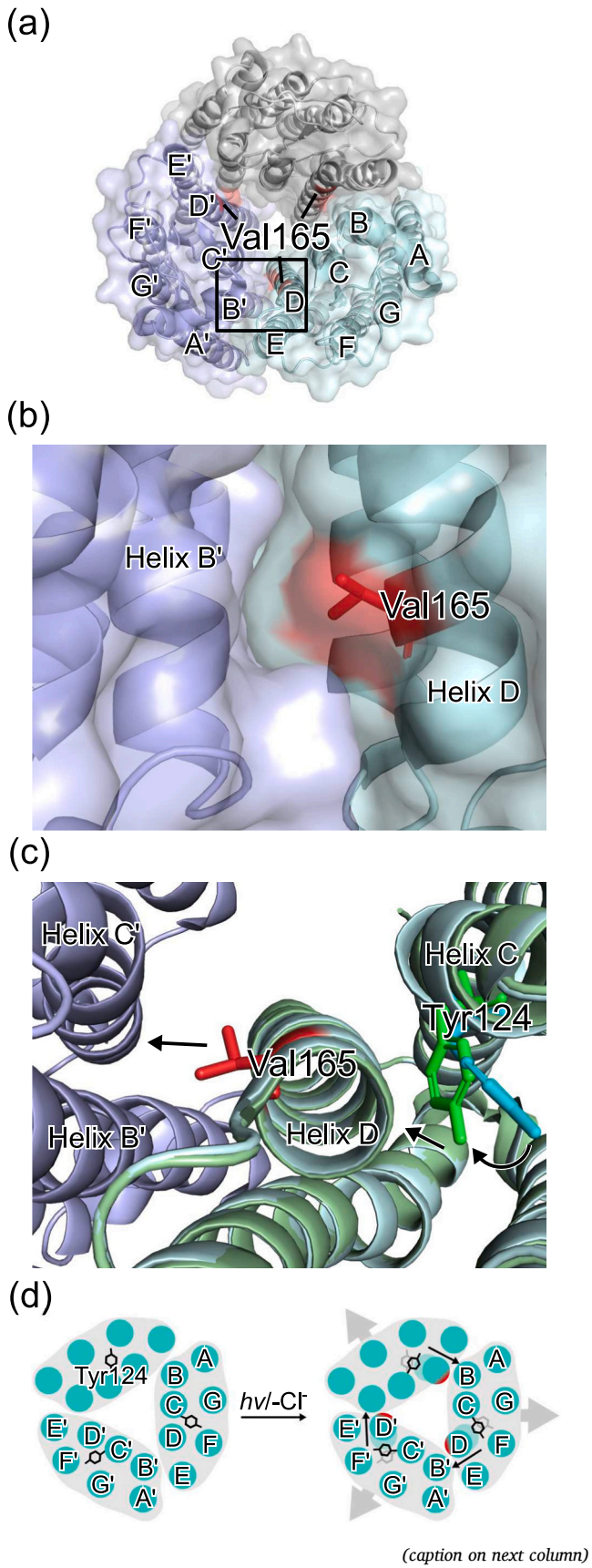

(caption on next column)

Fig. 8. The trimer dissociation scheme proposed for *Np*HR A165V mutant. (a) *Np*HR trimeric structure with the 165th position highlighted in red. (b) A lateral blow-up view at the trimer interface, in which the 165th residue is mutated to valine. The monomer structure is based on the Cl^--bound state *Np*HR (PDB entry 3A7K [22]). For the trimeric assembly, we used the homologous model from *Hs*HR (PDB entry 1E12 [66]) because the protein expressed in *E. coli* lacks bacterioruberin, which is necessary for the trimeric assembling in the 3A7K trimeric form [22,59]. (c and d) The proposed trimer dissociation mechanism for the A165V mutant. The Cl^--free O-like structure (green, PDB entry 3QBG [23]) is presented. The sidechain of Tyr124 rotates toward the helix D by Cl^- depletion or during the O intermediate formation in the photocycle, which may push the helix D outward and lead to the trimer dissociation. The structure visualization and the amino acid replacement for A165V were performed using PyMOL. (For interpretation of the references to colour in this figure legend, the reader is referred to the web version of this article.)

mutants. The structural instability suggested for the G163A mutant from the broadly distributed pSB ^{15}N signals both in the Cl^--bound and -free states may account for the less accumulated O-intermediate. Determination of the Cl^- binding affinity for the O-intermediate will be beneficial to improve this picture. Also, more details of the outward movement of the helix D such as its direction, associated structural events and its driving force should be clarified. As a possibility, the sidechain of Tyr124 is known to rotate toward the helix D by Cl^- depletion [23]. If this sidechain rotation were the driving force of the movement, mutation of Tyr124 to an amino acids with small sidechain would reduce the steric effect and may avoid the trimer disruption in the A165V mutant. To corroborate the steric effect played by the bulky valine sidechain at the 165th position it would be worth seeing if e.g., A165W mutant with even larger sidechain would disrupt the trimer integrity even in the Cl^--bound states.

At present, the insufficient coverage of chemical shift assignment humpers providing precise picture of the outward movement of helix D and other part of the protein. The assignment is difficult due to the nature of membrane proteins whose amino acid types are strongly biased toward the hydrophobic residues. Reverse isotope labeling, which was utilized in the assignment of proteorhodopsin [69] and sodium ion pump rhodopsin, KR2 [70] may be useful. Another solution would include the combination of the ^1H-detection fast-MAS ssNMR and high-dimensional spectroscopy, which successfully applied recently to a study on a large (>100 kDa) enzyme protein [71]. Development of better signal assignment protocol/strategies [72] and its application to membrane proteins is also to be made. Once the coverage of the signal assignment is improved, distance measurements between the monomers, angles measurements between helices and relative to the membrane normal, etc. would become possible for more detailed structural analysis. We would report on these efforts in the future publications.

Despite the remaining future works, we underline here that the analyses using ssNMR shown in this work showcased an important step forward in elucidating the function of *Np*HR, and is crucial, in general, for a detailed understanding of microbial rhodopsins in near physiological condition. We identified, for the first time, the importance of the EC part of helix D (including the 163rd and 165th amino acids) in the late photocycle. The amino acid mutation at these key residues both drastically perturbed the late photocycle related to the Cl^- ion uptake, which was attributed either to disordered protein conformation around retinal, or to the disruption of the physiological trimer. By combining (DNP-enhanced) ssNMR spectroscopy with mutation works, (transient) visible spectroscopy and crystallographic data in the literatures, we were able to propose a model for the Cl^- ion release/uptake step, that forms a basis for the future investigation.

5. Conclusion

In this study, we combined ssNMR spectroscopy with photochemical property analyses on WT and mutants of *Np*HR in lipid bilayer

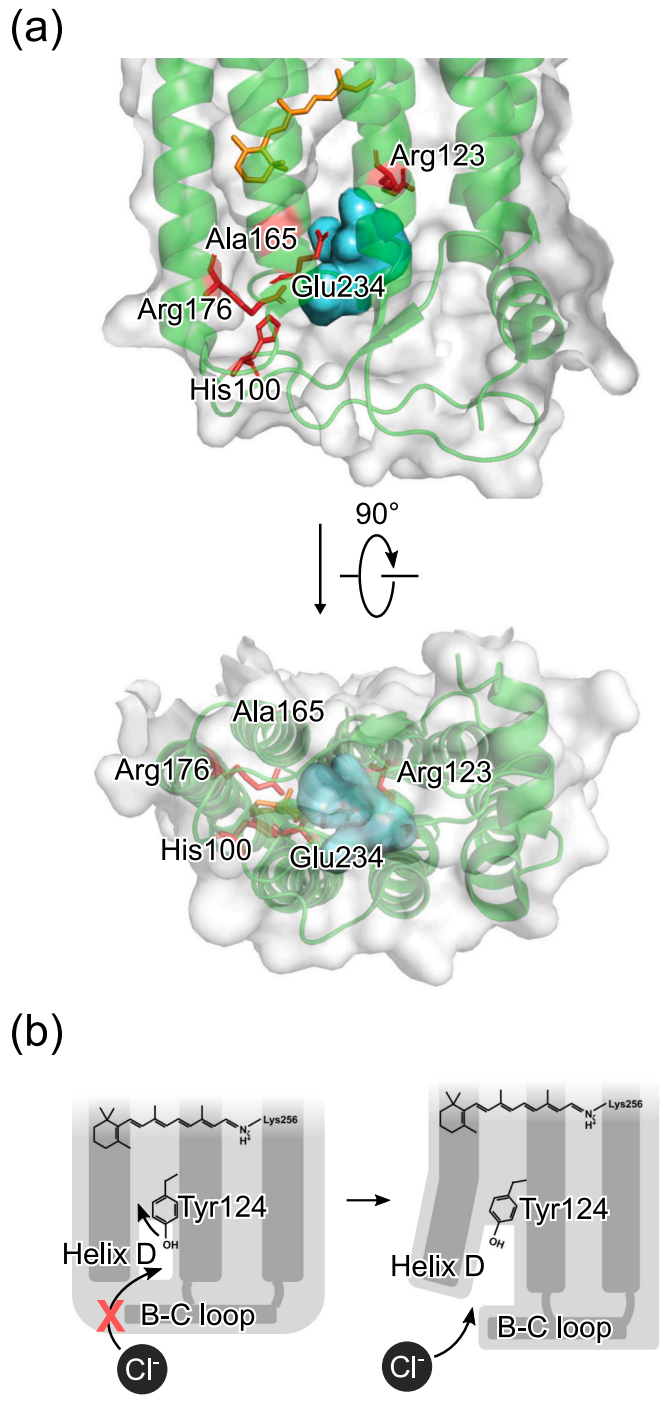

Fig. 9. The Cl^- uptake scheme of *Np*HR proposed in the present study. (a) Side view from the trimer interface side and the top view from the EC side of the Cl^--free blue form *Np*HR (PDB entry 3QBG [23]). The putative key residues for Cl^- uptake [22] and Ala165 are shown in red. The inter-helix space mentioned in the text is highlighted in cyan. The retinal is in orange. The protein structures are visualized using PyMOL. (b) Schematics for the Cl^- uptake process with the observed structural changes. The hydrophobic B-C loop covers the Cl^- entrance path in the Cl^--bound state and prevents the Cl^- uptake. The outward movement of helix D permits to expose the inter-helix space to solvent which allows the Cl^- to enter. (For interpretation of the references to colour in this figure legend, the reader is referred to the web version of this article.)

environment by focusing on the late photocycle, involving the Cl^- ion release/uptake step. Our ssNMR results suggested a major structural change in the EC part of the helix D between the Cl^--bound and -free states. Subsequent mutation works and spectroscopic analyses confirmed its importance in the Cl- uptake process. The data revealed the possibility of an outward movement in the EC part of the helix D and provided insights into the relationship between this structural change and the Cl^- uptake process. DNP-enhanced ^{15}N NMR spectroscopy elucidated the geometry changes around the protonated Schiff Bases, pointing out the existence of three principal substates in the O-intermediate. Our results filled the gap between the limited structural changes for *Np*HR observed by X-ray crystallography and the relatively large molecular volume change during photocycle claimed by spectroscopic studies in the literatures. Through this work, we would underline importance of ssNMR methods in the structural studies on membrane proteins, providing site-specific structural information in the near physiological conditions.

Authors contribution statement

The authors confirm contribution to the paper as follows: study conception and design: H.T., T.F., Y.M.; data collection: X.Z., H.T., T.K., Y.M.; analysis and interpretation of results: X.Z., H.T., Y.M.; draft manuscript preparation: X.Z., H.T., Y.M. All authors reviewed the results and approved the final version of the manuscript.

CRediT authorship contribution statement

Xin Zhang: Writing – original draft, Visualization, Validation, Investigation. **Hajime Tamaki:** Writing – review & editing, Investigation, Formal analysis, Data curation. **Takashi Kikukawa:** Investigation. **Toshimichi Fujiwara:** Writing – review & editing, Supervision, Funding acquisition. **Yoh Matsuki:** Writing – review & editing, Supervision, Project administration, Methodology, Investigation, Funding acquisition, Data curation, Conceptualization.

Declaration of competing interest

The authors declare that they have no known competing financial interests or personal relationships that could have appeared to influence the work reported in this paper.

Acknowledgements

This work was supported by JST Adaptable and Seamless Technology Transfer Program through Target-Driven R&D (A-STEP, JPMJTR204D) (H. T., Y. M.); JST OPERA JPMJOP1861 and JEOL YOKOGUSHI Research Alliance Laboratories of Osaka University. Authors thank to Dr. Ken Kato and Dr. Tomoaki Sugishita for their fruitful discussion and comments.

Appendix A. Supplementary data

Supplementary data to this article can be found online at https://doi.org/10.1016/j.bpc.2024.107329.

References

[1] B. Schobert, J.K. Lanyi, Halorhodopsin is a light-driven chloride pump, J. Biol. Chem. 257 (17) (1982) 10306–10313, https://doi.org/10.1016/S0021-9258(18)34020-1.
[2] H. Yawoo, H. Kandori, A. Koizumi, in: H. Yawo, H. Kandori, A. Koizumi (Eds.), Optogenetics, Springer Japan, 2015, https://doi.org/10.1007/978-4-431-55516-2.
[3] T. Motoyuki, N. Hazemoto, M. Kondo, N. Kamo, Y. Kobatake, Y. Terayama, Two photocycles in *halobacterium halobium* that lacks bacteriorhodopsin, Biochem. Biophys. Res. Commun. 108 (3) (1982) 970–976, https://doi.org/10.1016/0006-291X(82)92094-0.

[4] A. Matsuno-Yagi, Y. Mukohata, ATP synthesis linked to light-dependent proton uptake in a red mutant strain of halobacterium lacking bacteriorhodopsin, Arch. Biochem. Biophys. 199 (1) (1980) 297–303, https://doi.org/10.1016/0003-9861(80)90284-2.

[5] C. Engelhard, I. Chizhov, F. Siebert, M. Engelhard, Microbial halorhodopsins: light-driven chloride pumps, Chem. Rev. 118 (21) (2018) 10629–10645, https://doi.org/10.1021/acs.chemrev.7b00715.

[6] I.P. Hohenfeld, A.A. Wegener, M. Engelhard, Purification of histidine tagged bacteriorhodopsin, *pharaonis* halorhodopsin and *pharaonis* sensory rhodopsin II functionally expressed in *Escherichia coli*, FEBS Lett. 442 (2–3) (1999) 198–202, https://doi.org/10.1016/S0014-5793(98)01659-7.

[7] F. Zhang, L.P. Wang, M. Brauner, et al., Multimodal fast optical interrogation of neural circuitry, Nature 446 (7136) (2007) 633–639, https://doi.org/10.1038/nature05744.

[8] G. Varo, L.S. Brown, J. Sasaki, et al., Light-driven chloride ion transport by halorhodopsin from *Natronobacterium pharaonis*. I. The photochemical cycle, Biochemistry 34 (44) (1995) 14490–14499, https://doi.org/10.1021/bi00044a027.

[9] T. Kouyama, H. Kawaguchi, T. Nakanishi, H. Kubo, M. Murakami, Crystal structures of the L_1, L_2, N, and O states of pharaonis halorhodopsin, Biophys. J. 108 (11) (2015) 2680–2690, https://doi.org/10.1016/j.bpj.2015.04.027.

[10] G. Varo, R. Needleman, J.K. Lanyi, Light-driven chloride ion transport by halorhodopsin from *Natronobacterium pharaonis*. II. Chloride release and uptake, protein conformation change, and thermodynamics, Biochemistry 34 (44) (1995) 14500–14507, https://doi.org/10.1021/bi00044a028.

[11] T. Kikukawa, C. Kusakabe, A. Kokubo, et al., Probing the Cl−pumping photocycle of pharaonis halorhodopsin: examinations with bacterioruberin, an intrinsic dye, and membrane potential-induced modulation of the photocycle, Biochim. Biophys. Acta Bioenerg. 1847 (8) (2015) 748–758, https://doi.org/10.1016/j.bbabio.2015.05.002.

[12] M. Shibata, Y. Saito, M. Demura, H. Kandori, Deprotonation of Glu234 during the photocycle of *Natronomonas pharaonis* halorhodopsin, Chem. Phys. Lett. 432 (4–6) (2006) 545–547, https://doi.org/10.1016/j.cplett.2006.10.111.

[13] K. Shibasaki, H. Shigemura, T. Kikukawa, et al., Role of Thr218 in the light-driven anion pump halorhodopsin from *Natronomonas pharaonis*, Biochemistry 52 (51) (2013) 9257–9268, https://doi.org/10.1021/bi401295e.

[14] M. Kubo, T. Kikukawa, S. Miyauchi, et al., Role of Arg123 in light-driven anion pump mechanisms of *pharaonis* halorhodopsin, Photochem. Photobiol. 85 (2) (2009) 547–555, https://doi.org/10.1111/j.1751-1097.2009.00538.x.

[15] M. Sato, T. Kikukawa, T. Araiso, et al., Ser-130 of *Natronobacterium pharaonis* halorhodopsin is important for the chloride binding, Biophys. Chem. 104 (1) (2003) 209–216, https://doi.org/10.1016/S0301-4622(02)00368-X.

[16] M. Sato, Roles of Ser130 and Thr126 in chloride binding and photocycle of pharaonis halorhodopsin, J. Biochem. 134 (1) (2003) 151–158, https://doi.org/10.1093/jb/mvg123.

[17] M. Sato, M. Kubo, T. Aizawa, et al., Role of putative anion-binding sites in cytoplasmic and extracellular channels of *Natronomonas pharaonis* halorhodopsin, Biochemistry 44 (12) (2005) 4775–4784, https://doi.org/10.1021/bi047500f.

[18] M. Sato, M. Kubo, T. Aizawa, et al., Role of putative anion-binding sites in cytoplasmic and extracellular channels of *Natronomonas pharaonis* halorhodopsin, Biochemistry 44 (12) (2005) 4775–4784, https://doi.org/10.1021/bi047500f.

[19] M. Sato, T. Kanamori, N. Kamo, M. Demura, K. Nitta, Stopped-flow analysis on anion binding to blue-form halorhodopsin from *Natronobacterium pharaonis*: comparison with the anion-uptake process during the photocycle, Biochemistry 41 (7) (2002) 2452–2458, https://doi.org/10.1021/bi011788g.

[20] K. Inoue, M. Kubo, M. Demura, N. Kamo, M. Terazima, Reaction dynamics of halorhodopsin studied by time-resolved diffusion, Biophys. J. 96 (9) (2009) 3724–3734, https://doi.org/10.1016/j.bpj.2008.12.3932.

[21] K. Ihara, A. Narusawa, K. Maruyama, M. Takeguchi, T. Kouyama, A halorhodopsin-overproducing mutant isolated from an extremely haloalkaliphilic archaeon *Natronomonas pharaonis*, FEBS Lett. 582 (19) (2008) 2931–2936, https://doi.org/10.1016/j.febslet.2008.07.030.

[22] T. Kouyama, S. Kanada, Y. Takeguchi, A. Narusawa, M. Murakami, K. Ihara, Crystal structure of the light-driven chloride pump halorhodopsin from *Natronomonas pharaonis*, J. Mol. Biol. 396 (3) (2010) 564–579, https://doi.org/10.1016/j.jmb.2009.11.061.

[23] S. Kanada, Y. Takeguchi, M. Murakami, K. Ihara, T. Kouyama, Crystal structures of an O-like blue form and an anion-free yellow form of pharaonis halorhodopsin, J. Mol. Biol. 413 (1) (2011) 162–176, https://doi.org/10.1016/j.jmb.2011.08.021.

[24] J. Guijarro, M. Engelhard, F. Siebert, Anion uptake in halorhodopsin from natromonas pharaonis studied by FTIR spectroscopy: consequences for the anion transport mechanism, Biochemistry 45 (38) (2006) 11578–11588, https://doi.org/10.1021/bi060753j.

[25] C. Hackmann, J. Guijarro, I. Chizhov, M. Engelhard, C. Rödig, F. Siebert, Static and time-resolved step-scan Fourier transform infrared investigations of the photoreaction of halorhodopsin from *Natronobacterium Pharaonis*: consequences for models of the anion translocation mechanism, Biophys. J. 81 (1) (2001) 394–406, https://doi.org/10.1016/S0006-3495(01)75708-6.

[26] V. Ladizhansky, Applications of solid-state NMR to membrane proteins, Biochim. Biophys. Acta, Proteins Proteomics 1865 (11) (2017) 1577–1586, https://doi.org/10.1016/j.bbapap.2017.07.004.

[27] C.N. Kriebel, J. Becker-Baldus, C. Glaubitz, Solid-state NMR spectroscopy on microbial rhodopsins, in: Methods in Molecular Biology vol. 2501, Humana Press Inc., 2022, pp. 181–206, https://doi.org/10.1007/978-1-0716-2329-9_9.

[28] M.E. Ward, L.S. Brown, V. Ladizhansky, Advanced solid-state NMR techniques for characterization of membrane protein structure and dynamics: application to Anabaena sensory rhodopsin, J. Magn. Reson. 253 (2015) 119–128, https://doi.org/10.1016/j.jmr.2014.11.017.

[29] D.B. Good, S. Wang, M.E. Ward, et al., Conformational dynamics of a seven transmembrane helical protein Anabaena sensory rhodopsin probed by solid-state NMR, J. Am. Chem. Soc. 136 (7) (2014) 2833–2842, https://doi.org/10.1021/ja411633w.

[30] S. Wang, R.A. Munro, L. Shi, et al., Solid-state NMR spectroscopy structure determination of a lipid-embedded heptahelical membrane protein, Nat. Methods 10 (10) (2013) 1007–1012, https://doi.org/10.1038/nmeth.2635.

[31] N. Pfleger, A.C. Wörner, J. Yang, et al., Solid-state NMR and functional studies on proteorhodopsin, Biochim. Biophys. Acta 1787 (6) (2009) 697–705, https://doi.org/10.1016/j.bbabio.2009.02.022.

[32] N. Pfleger, M. Lorch, A.C. Woerner, S. Shastri, C. Glaubitz, Characterisation of Schiff base and chromophore in green proteorhodopsin by solid-state NMR, J. Biomol. NMR 40 (1) (2008) 15–21, https://doi.org/10.1007/s10858-007-9203-5.

[33] Y. Makino, I. Kawamura, T. Okitsu, et al., Retinal configuration of ppR intermediates revealed by photoirradiation solid-state NMR and DFT, Biophys. J. 115 (1) (2018) 72–83, https://doi.org/10.1016/j.bpj.2018.05.030.

[34] V.S. Bajaj, M.L. Mak-Jurkauskas, M. Belenky, J. Herzfeld, R.G. Griffin, Functional and shunt states of bacteriorhodopsin resolved by 250 GHz dynamic nuclear polarization–enhanced solid-state NMR, Proc. Natl. Acad. Sci. 106 (23) (2009) 9244–9249, https://doi.org/10.1073/pnas.0900908106.

[35] S. Kumagai, I. Kawamura, Solid-state NMR of the retinal protonated Schiff base in microbial rhodopsins, Magn. Reson. Lett. (April 25, 2024) 200132, https://doi.org/10.1016/j.mrl.2024.200132. Published online.

[36] K. Kajimoto, T. Kikukawa, H. Nakashima, et al., Transient resonance Raman spectroscopy of a light-driven sodium-ion-pump rhodopsin from *Indibacter alkaliphilus*, J. Phys. Chem. B 121 (17) (2017) 4431–4437, https://doi.org/10.1021/acs.jpcb.7b02421.

[37] B. Scharf, M. Engelhard, Blue halorhodopsin from *Natronobacterium pharaonis*: wavelength regulation by anions, Biochemistry 33 (21) (1994) 6387–6393, https://doi.org/10.1021/BI00187A002.

[38] A. Böckmann, C. Gardiennet, R. Verel, et al., Characterization of different water pools in solid-state NMR protein samples, J. Biomol. NMR 45 (3) (2009) 319–327, https://doi.org/10.1007/s10858-009-9374-3.

[39] K.R. Thurber, R. Tycko, Measurement of sample temperatures under magic-angle spinning from the chemical shift and spin-lattice relaxation rate of ^{79}Br in KBr powder, J. Magn. Reson. 196 (1) (2009) 84–87, https://doi.org/10.1016/j.jmr.2008.09.019.

[40] M. Baldus, A.T. Petkova, J. Herzfeld, R.G. Griffin, Cross polarization in the tilted frame: assignment and spectral simplification in heteronuclear spin systems, Mol. Phys. 95 (6) (1998) 1197–1207, https://doi.org/10.1080/00268979809483251.

[41] J. Pauli, M. Baldus, B. van Rossum, H. de Groot, H. Oschkinat, Backbone and side-chain ^{13}C and ^{15}N signal assignments of the α-spectrin SH3 domain by magic angle spinning solid-state NMR at 17.6 tesla, ChemBioChem 2 (4) (2001) 272–281, https://doi.org/10.1002/1439-7633(20010401)2:4<272::AID-CBIC272>3.0.CO;2-2.

[42] Y. Li, D.A. Berthold, H.L. Frericks, R.B. Gennis, C.M. Rienstra, Partial ^{13}C and ^{15}N chemical-shift assignments of the disulfide-bond-forming enzyme DsbB by 3D magic-angle spinning NMR spectroscopy, ChemBioChem 8 (4) (2007) 434–442, https://doi.org/10.1002/cbic.200600484.

[43] W.T. Franks, K.D. Kloepper, B.J. Wylie, C.M. Rienstra, Four-dimensional heteronuclear correlation experiments for chemical shift assignment of solid proteins, J. Biomol. NMR 39 (2) (2007) 107–131, https://doi.org/10.1007/s10858-007-9179-1.

[44] A. Schuetz, C. Wasmer, B. Habenstein, et al., Protocols for the sequential solid-state NMR spectroscopic assignment of a uniformly labeled 25 kDa protein: HET-s(1-227), ChemBioChem 11 (11) (2010) 1543–1551, https://doi.org/10.1002/cbic.201000124.

[45] C.R. Morcombe, K.W. Zilm, Chemical shift referencing in MAS solid state NMR, J. Magn. Reson. 162 (2) (2003) 479–486, https://doi.org/10.1016/S1090-7807(03)00082-X.

[46] J.L. Markley, A. Bax, Y. Arata, et al., Recommendations for the presentation of NMR structures of proteins and nucleic acids, Eur. J. Biochem. 256 (1) (1998) 1–15, https://doi.org/10.1046/j.1432-1327.1998.2560001.x.

[47] F. Delaglio, S. Grzesiek, W. Vuister Geerten, G. Zhu, J. Pfeifer, A. Bax, NMRPipe: a multidimensional spectral processing system based on UNIX pipes, J. Biomol. NMR 6 (3) (1995) 277–293, https://doi.org/10.1007/BF00197809.

[48] W. Lee, M. Tonelli, J.L. Markley, NMRFAM-SPARKY: enhanced software for biomolecular NMR spectroscopy, Bioinformatics 31 (8) (2015) 1325–1327, https://doi.org/10.1093/bioinformatics/btu830.

[49] S.P. Skinner, R.H. Fogh, W. Boucher, T.J. Ragan, L.G. Mureddu, G.W. Vuister, CcpNmr AnalysisAssign: a flexible platform for integrated NMR analysis, J. Biomol. NMR 66 (2) (2016) 111–124, https://doi.org/10.1007/s10858-016-0060-y.

[50] E. Schmidt, P. Güntert, A new algorithm for reliable and general NMR resonance assignment, J. Am. Chem. Soc. 134 (30) (2012) 12817–12829, https://doi.org/10.1021/ja305091n.

[51] E. Schmidt, J. Gath, B. Habenstein, et al., Automated solid-state NMR resonance assignment of protein microcrystals and amyloids, J. Biomol. NMR 56 (3) (2013) 243–254, https://doi.org/10.1007/s10858-013-9742-x.

[52] T. Kikukawa, C.K. Saha, S.P. Balashov, et al., The lifetimes of *Pharaonis* phoborhodopsin signaling states depend on the rates of proton transfers—effects of hydrostatic pressure and stopped flow experiments, Photochem. Photobiol. 84 (4) (2008) 880–888, https://doi.org/10.1111/j.1751-1097.2008.00318.x.

[53] C. Hasegawa, T. Kikukawa, S. Miyauchi, et al., Interaction of the halobacterial transducer to a halorhodopsin mutant engineered so as to bind the transducer: Cl^- circulation within the extracellular channel†, Photochem. Photobiol. 83 (2) (2007) 293–302, https://doi.org/10.1562/2006-06-09-RA-916.
[54] C. Sauvée, M. Rosay, G. Casano, et al., Highly efficient, water-soluble polarizing agents for dynamic nuclear polarization at high frequency, Angew. Chem. Int. Ed. 52 (41) (2013) 10858–10861, https://doi.org/10.1002/anie.201304657.
[55] Y. Matsuki, S. Nakamura, S. Fukui, H. Suematsu, T. Fujiwara, Closed-cycle cold helium magic-angle spinning for sensitivity-enhanced multi-dimensional solid-state NMR, J. Magn. Reson. 259 (2015) 76–81, https://doi.org/10.1016/j.jmr.2015.08.003.
[56] V.A. Higman, J. Flinders, M. Hiller, et al., Assigning large proteins in the solid state: a MAS NMR resonance assignment strategy using selectively and extensively ^{13}C-labelled proteins, J. Biomol. NMR 44 (4) (2009) 245–260, https://doi.org/10.1007/s10858-009-9338-7.
[57] F. Castellani, B. van Rossum, A. Diehl, M. Schubert, K. Rehbein, H. Oschkinat, Structure of a protein determined by solid-state magic-angle-spinning NMR spectroscopy, Nature 420 (6911) (2002) 99–102, https://doi.org/10.1038/nature01070.
[58] I. Chizhov, M. Engelhard, Temperature and halide dependence of the photocycle of halorhodopsin from *Natronobacterium pharaonis*, Biophys. J. 81 (3) (2001) 1600–1612, https://doi.org/10.1016/S0006-3495(01)75814-6.
[59] T. Tsukamoto, T. Sasaki, K.J. Fujimoto, et al., Homotrimer formation and dissociation of pharaonis halorhodopsin in detergent system, Biophys. J. 102 (12) (2012) 2906–2915, https://doi.org/10.1016/j.bpj.2012.05.008.
[60] Q.Z. Ni, E. Daviso, T.V. Can, et al., High frequency dynamic nuclear polarization, Acc. Chem. Res. 46 (9) (2013) 1933–1941, https://doi.org/10.1021/ar300348n.
[61] A.B. Barnes, M.L. Mak-Jurkauskas, Y. Matsuki, et al., Cryogenic sample exchange NMR probe for magic angle spinning dynamic nuclear polarization, J. Magn. Reson. 198 (2) (2009) 261–270, https://doi.org/10.1016/j.jmr.2009.03.003.
[62] Q.Z. Ni, E. Markhasin, T.V. Can, et al., Peptide and protein dynamics and low-temperature/DNP magic angle spinning NMR, J. Phys. Chem. B 121 (19) (2017) 4997–5006, https://doi.org/10.1021/acs.jpcb.7b02066.
[63] J.G. Hu, B.Q. Sun, A.T. Petkova, R.G. Griffin, J. Herzfeld, The predischarge chromophore in bacteriorhodopsin: a ^{15}N solid-state NMR study of the L photointermediate, Biochemistry 36 (31) (1997) 9316–9322, https://doi.org/10.1021/bi970416y.
[64] J. Hu, R.G. Griffin, J. Herzfeld, Synergy in the spectral tuning of retinal pigments: complete accounting of the opsin shift in bacteriorhodopsin, Proc. Natl. Acad. Sci. 91 (19) (1994) 8880–8884, https://doi.org/10.1073/pnas.91.19.8880.
[65] A.F.L. Creemers, C.H.W. Klaassen, P.H.M. Bovee-Geurts, et al., Solid state ^{15}N NMR evidence for a complex Schiff base counterion in the visual G-protein-coupled receptor rhodopsin, Biochemistry 38 (22) (1999) 7195–7199, https://doi.org/10.1021/bi9830157.
[66] M. Kolbe, H. Besir, L.O. Essen, D. Oesterhelt, Structure of the light-driven chloride pump halorhodopsin at 1.8 Å resolution, Science 288 (5470) (2000) 1390–1396, https://doi.org/10.1126/science.288.5470.1390.
[67] M. Karasuyama, K. Inoue, R. Nakamura, H. Kandori, I. Takeuchi, Understanding colour tuning rules and predicting absorption wavelengths of microbial rhodopsins by data-driven machine-learning approach, Sci. Rep. 8 (1) (2018) 15580, https://doi.org/10.1038/s41598-018-33984-w.
[68] H.E. Kato, M. Kamiya, S. Sugo, et al., Atomistic design of microbial opsin-based blue-shifted optogenetics tools, Nat. Commun. 6 (1) (2015) 7177, https://doi.org/10.1038/ncomms8177.
[69] L. Shi, E.M.R. Lake, M.A.M. Ahmed, L.S. Brown, V. Ladizhansky, Solid-state NMR study of proteorhodopsin in the lipid environment: secondary structure and dynamics, Biochim. Biophys. Acta Biomembr. 1788 (12) (2009) 2563–2574, https://doi.org/10.1016/j.bbamem.2009.09.011.
[70] J. Kaur, C.N. Kriebel, P. Eberhardt, et al., Solid-state NMR analysis of the sodium pump Krokinobacter rhodopsin 2 and its H30A mutant, J. Struct. Biol. 206 (1) (2019) 55–65, https://doi.org/10.1016/j.jsb.2018.06.001.
[71] A. Klein, P. Rovó, V.V. Sakhrani, et al., Atomic-resolution chemical characterization of (2x)72-kDa tryptophan synthase via four- and five-dimensional ^{1}H-detected solid-state NMR, Proc. Natl. Acad. Sci. 119 (4) (2022) e2114690119, https://doi.org/10.1073/pnas.2114690119.
[72] H. Tamaki, Y. Matsuki, Optimal-control-based Cβ chemical shift encoding for efficient signal assignment of solid proteins, J. Phys. Chem. B 127 (47) (2023) 10118–10128, https://doi.org/10.1021/acs.jpcb.3c05914.